Johann Radon Institute for
Computational and Applied Mathematics
Austrian Academy of Sciences (ÖAW)

A Numerical Study on a Preconditioned GMRES Solver with Algebraic Multigrid Accelerations for the Fluid-Structure Interaction Problems on Hybrid Meshes

H. Yang

RICAM-Report 2011-15

A Numerical Study on a Preconditioned GMRES Solver with Algebraic Multigrid Accelerations for the Fluid-Structure Interaction Problems on Hybrid Meshes

Huidong Yang[a,1]

[a] *Austrian Academy of Sciences,*
Johann Radon Institute for Computational and Applied Mathematics,
Altenberger Strasse 69, A-4040 Linz, Austria

Abstract

In this work, we propose a preconditioned GMRES solver for a Schur complement equation of the linearized fluid-structure interaction problem, with respect to the displacement unknowns only on the interface. The preconditioning for the Schur complement equation requires approximate solutions of the fluid and structure sub-problems with appropriate boundary conditions on the interface, in particular, a Robin condition for the fluid problem and a Neumann condition for the structure problem. Both sub-problems are spatially discretized by a finite element method on hybrid meshes and temporally discretized by implicit first-order methods. The discretized equations of both sub-problems are solved by special algebraic multigrid methods. The performance of this preconditioned GMRES solver is compared with that of a Newton based fluid-structure interaction solver. The convergence dependence on different parameters is studied by numerical experiments.

Keywords: fluid-structure interaction, Schur complement equation, RN preconditioned GMRES, algebraic multigrid methods, finite element methods, extended P_1 element, hybrid meshes
2010 MSC: 37M05, 65N30, 65N55, 74F10

[1] huidong.yang@oeaw.ac.at

July 6, 2011

1. Introduction

In our recent work of [28, 26, 25, 27, 18], two main contributions to the partitioned Newton based solver for solving the nonlinear fluid-structure interaction (FSI) problems have been made: an extended P_1 finite element discretization of the structure and fluid sub-problems on hybrid meshes containing tetrahedral, hexahedral, prismatic and pyramidic elements; special algebraic multigrid (AMG) methods for solving the discretized fluid and structure sub-problems on such meshes. As is well known, the Newton iteration in the FSI problem requires inversions of Jacobians of the so-called Steklo-Poincaré operators, which are usually approximated by the GMRES solver (see [9, 10, 21]). In each GMRES iteration, the Jacobians are computed analytically since simple approximations might seriously deteriorate the convergence (see [28] and the reference therein). Therefore, the cost for each Newton iteration is quite expensive. However, the overall cost is able to be compensated by a quadratic convergence of the Newton iterations, see e.g., [10] for performance measurements. It is worth mentioning the work of [4], where a parallel Newton solver under the domain decomposition framework is considered to improve the performance.

In comparison with the Newton based FSI solver, the conventional fixed-poit FSI solver is easier to implement, and often leads to an efficient one with appropriate dynamic relaxations, see e.g. [17]. Among them is the most popular Dirichlet-Neumann (DN) iterations. Unluckily such methods suffer from the so-called added-mass effect and extremely slow convergence in certain situations, see e.g., [8]. One of recent improvements in this direction has been proposed in [2, 3], where the Dirichlet and Neumann conditions in the DN iterations are replaced by Robin-Robin (RR) transmission conditions. In particular we consider a Robin-Neumann (RN) preconditioned GMRES solver. To the author's best knowledge, this has not been applied to our FSI problems where hybrid meshes and special algebraic multigrid methods for sub-problems are used. On the other hand, under such situations, a computational comparison of the Newton based and the RN preconditioned GMRES solvers is not available. These points will be considered in this piece of work. Furthermore, we reformulate a Schur complement equation of the linearized FSI problem, with respect to the structure displacement on the interface instead of the structure velocity used in [3]. This allows us to reuse the pre-existing fluid and structure codes developed in the work of [25], in a straightforward way. The convergence dependence on the Robin weighting

parameter, the time step size, the geometry of a computational domain and the material parameters is also investigated from a numerical point of view.

The reminder of this paper is organized in the following way. In Section 2, we set up a FSI problem on the continuous level. Section 3 deals with the linearization, the time discretization, and the extended P_1 element on hybrid meshes applied to both sub-problems with RN transmission conditions on the interface. Section 4 describes the RN preconditioned GMRES solver to the Schur complement equation with respect to the displacement unknowns. The applications of special AMG methods for both sub-problems are demonstrated in Section 5. Finally, in Section 6, a few numerical results are presented.

2. A FSI problem

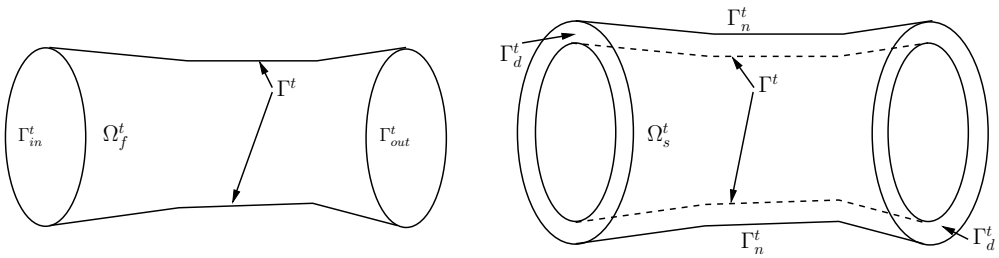

Figure 1: A schematic representation of a computational domain Ω^t: fluid domain Ω^t_f (left) and structure domain Ω^t_s (right).

The computational fluid-structure domain $\Omega^t \subset \mathbb{R}^3$ is decomposed into the deformable structure sub-domain Ω^t_s and the fluid sub-domain Ω^t_f:

$$\overline{\Omega^t} = \overline{\Omega^t_s} \cup \overline{\Omega^t_f},$$

where t denotes the time, and the subscripts s and f represent the structure and the fluid, respectively. The interface Γ^t is an intersection between boundaries of Ω^t_s and Ω^t_f:

$$\Gamma^t = \partial\Omega^t_s \cap \partial\Omega^t_f.$$

In addition, Γ^t_{in} and Γ^t_{out} denote the in-flow and out-flow boundaries of Ω^t_f, respectively, and Γ^t_d and Γ^t_n denote the boundaries of Ω^t_s with Dirichlet and Neumann boundary conditions, respectively. At $t = 0$, we have the initial

(reference) configurations: Ω_s^0, Ω_f^0, Γ^0, Γ_{in}^0, Γ_{out}^0, Γ_d^0 and Γ_n^0. See Fig. 1 for an illustration.

The evolution of the domain Ω^t is obtained by two families of mappings:

$$\mathcal{L} : \Omega_s^0 \times (0,T) \to \Omega_s^t,\ (x_0,t) \mapsto x = \mathcal{L}(x_0,t) =: \mathcal{L}^t(x_0) \text{ for all } x_0 \in \Omega_s^0,$$

$$\mathcal{A} : \Omega_f^0 \times (0,T) \to \Omega_f^t,\ (x_0,t) \mapsto x = \mathcal{A}(x_0,t) =: \mathcal{A}^t(x_0) \text{ for all } x_0 \in \Omega_f^0.$$

For the structure problem on the Lagrangian framework, the mapping $\mathcal{L}^t$ is given by

$$\mathcal{L}^t(x_0) = x_0 + \hat{d}_s(x_0,t),$$

where $\hat{d}_s(x_0,t)$ denotes the displacement of the structure domain at time t.

For the fluid problem, an arbitrary Lagrangian-Eulerian (ALE) framework (see [11]) is used:

$$\mathcal{A}^t(x_0) = x_0 + \hat{d}_f(x_0,t),$$

where $\hat{d}_f(x_0,t)$ denotes the displacement of the fluid domain at time t, and is typically defined as a harmonic extension $\hat{d}_f = \mathrm{Ext}(\hat{d}_s|_{\Gamma^0})$ of the structure displacement on Γ_0:

$$-\Delta \hat{d}_f = 0 \quad \text{in } \Omega_f^0, \tag{1a}$$

$$\hat{d}_f = 0 \quad \text{on } \Gamma_{in}^0 \cup \Gamma_{out}^0, \tag{1b}$$

$$\hat{d}_f = \hat{d}_s \quad \text{on } \Gamma^0. \tag{1c}$$

We also introduce

$$\hat{w}_s := \partial_t \mathcal{L}^t = \partial_t \hat{d}_s \text{ and } \hat{w}_f := \partial_t \mathcal{A}^t = \partial_t \hat{d}_f$$

for the structure and fluid domain velocities, respectively.

For evaluating the time derivative of a function g on the moving domain Ω_f^t, we define the ALE time derivative

$$\partial_t g|_{x_0} : \Omega_f^t \times (0,T) \to \mathbb{R},\ \partial_t g|_{x_0}(x,t) = \partial_t (g \circ \mathcal{A}^t) \circ \mathcal{A}^{t^{-1}}(x) = \frac{\partial g}{\partial t} + (w_f \cdot \nabla) g,$$

where $w_f(x,t) = \hat{w}_f \circ \mathcal{A}^{t^{-1}}$.

Then the coupled system of the FSI problem in strong form reads: Find the fluid velocity $u = u(x,t)$ and pressure $p = p(x,t)$, and the structure displacement $\hat{d}_s = \hat{d}_s(x_0,t)$ such that

$$\begin{aligned}
\rho_f \partial_t u|_{x_0} + \rho_f((u - w_f)\cdot\nabla)u - \nabla\cdot\sigma_f(u,p) &= 0 && \text{in } \Omega_f^t \times (0,T), && \text{(2a)}\\
\nabla\cdot u &= 0 && \text{in } \Omega_f^t \times (0,T), && \text{(2b)}\\
\sigma_f(u,p)n_f &= g_{in}^t && \text{on } \Gamma_{in}^t, && \text{(2c)}\\
\sigma_f(u,p)n_f &= 0 && \text{on } \Gamma_{out}^t, && \text{(2d)}\\
\rho_s \partial_t^2 \hat{d}_s - \nabla\cdot\hat{\sigma}_s(\hat{d}_s) &= 0 && \text{in } \Omega_s^0 \times (0,T), && \text{(2e)}\\
\hat{\sigma}_s(\hat{d}_s)\hat{n}_s &= 0 && \text{on } \Gamma_n^0, && \text{(2f)}\\
\hat{d}_s &= 0 && \text{on } \Gamma_d^0, && \text{(2g)}\\
u\circ\mathcal{A}^t &= \partial_t \hat{d}_s && \text{on } \Gamma^0, && \text{(2h)}\\
\sigma_f(u,p)n_f\circ\mathcal{A}^t + \hat{\sigma}_s(\hat{d}_s)\hat{n}_s &= 0 && \text{on } \Gamma^0, && \text{(2i)}
\end{aligned}$$

and

$$\Omega_f^t = \mathcal{A}^t(\Omega_f^0). \tag{3}$$

Here ρ_f and ρ_s denote the fluid and structure densities, respectively, and n_f and $\hat{n}_s$ are the outward normals to Ω_f^t and Ω_s^0, respectively.

In particular the Cauchy stress tensor for the Newtonian and incompressible flow is given by

$$\sigma_f(u,p) = -pI + 2\mu\varepsilon(u),$$

where μ is the fluid dynamic viscosity and $\varepsilon(u) = \frac{1}{2}(\nabla u + (\nabla u)^T)$ the strain rate tensor. The Neumann boundary condition on Γ_{in}^t is given by a function g_{in}^t.

For the structure, the linear Saint Venant-Kirchhoff elastic model is used

$$\hat{\sigma}_s(\hat{d}_s) = 2\mu^l\varepsilon(\hat{d}_s) + \lambda^l\nabla\cdot\hat{d}_s I$$

where μ^l and λ^l are Lamé constants, and $\varepsilon(\hat{d}_s) = \frac{1}{2}(\nabla\hat{d}_s + (\nabla\hat{d}_s)^T)$.

For the fluid (2a) and (2b) state the momentum balance and mass conservation laws, respectively. For the structure, (2e) states the momentum balance law. A no-slip condition and an equilibrium of the traction on Γ^0 are given by (2h) and (2i), respectively. The remaining conditions (2c), (2d), (2g) and (2f) are prescribed corresponding boundary conditions for the fluid and structure sub-problems. In addition, a geometrical problem (3) has to be solved at time t. It is easy to see that besides the nonlinearity from the

convection part in (2a), the geometrical nonlinearity causes another difficulty for solving the coupled FSI problem. To complete the problem, the following initial conditions are prescribed: $u(x_0, 0) = 0$, $\hat{d}_s(x_0, 0) = 0$, $\hat{w}_s(x_0, 0) = 0$.

3. Linearization, discretization, and the RN partitioned FSI system

3.1. Time discretization and linearization

For the time discretization of the FSI system (2), we follow the strategy in [28, 9], where an implicit Euler scheme for the fluid and a first order Newmark method for the structure are used. The nonlinear convective term is treated in a semi-implicit way as in [10, 28]. The geometrical nonlinearity is handled by a first order extrapolation, see e.g., [2].

Let Δt be the time step size and $t^n = n\Delta t, n \in \{0, 1, .., N\}$ be the time level at n. Let z^n be an approximation of a function z for the time level t^n. The standard backward difference operator $\delta_t(\cdot)$ is given by

$$\delta_t z^{n+1} = (z^{n+1} - z^n)/\Delta t$$

for the time level t^{n+1}.

The time discretized system reads (for simplicity of notations, we do not include the boundary conditions): Given u^n, $\hat{d}_s^n$, $\hat{w}_s^n$ and Ω_f^n, find u^{n+1}, p^{n+1}, and $\hat{d}_s^{n+1}$ such that

$$\begin{aligned}
\rho_f \delta_t u^{n+1}|_{x_0} + \rho_f((u^* - w_f^*) \cdot \nabla)u^{n+1} - \nabla \cdot \sigma_f(u^{n+1}, p^{n+1}) &= 0 \qquad \text{in } \Omega_f^*, \\
\nabla \cdot u^{n+1} &= 0 \qquad \text{in } \Omega_f^*, \\
\rho_s \delta_{tt} \hat{d}_s^{n+1} - \nabla \cdot \hat{\sigma}_s(\hat{d}_s^{n+1}) &= 0 \qquad \text{in } \Omega_s^0, \\
u^{n+1} \circ \mathcal{A}^* &= \delta_t \hat{d}_s^{n+1} \quad \text{on } \Gamma^0, \\
\sigma_f(u^{n+1}, p^{n+1}) n_f \circ \mathcal{A}^* + \hat{\sigma}_s(\hat{d}_s^{n+1}) \hat{n}_s &= 0 \qquad \text{on } \Gamma^0,
\end{aligned} \tag{4}$$

where

$$\delta_t z^{n+1}|_{x_0} = (z^{n+1} - z^n \circ \mathcal{A}^n \circ \mathcal{A}^{*-1})/\Delta t$$

is the backward difference for the ALE time derivative,

$$\delta_{tt} \hat{d}_s^{n+1} = 2(\hat{d}_s^{n+1} - \hat{d}_s^n)/\Delta t^2 - 2\hat{w}_s^n/\Delta t,$$

$\mathcal{A}^* = \mathcal{A}^n$, $\Omega_f^* = \Omega_f^n$, $u^* = u^n$ and $w_f^* = w_f^n$. The following updates are necessary for the next time level

$$\hat{d}_f^{n+1} = \mathrm{Ext}(\hat{d}_s^{n+1}|_{\Gamma^0}), \quad \Omega_f^{n+1} = \mathcal{A}^{n+1}(\Omega_f^0),$$

$$w_f^{n+1} = \delta_t \hat{d}_f^{n+1} \circ \mathcal{A}^{n+1^{-1}}, \quad \hat{w}_s^{n+1} = 2(\hat{d}_s^{n+1} - \hat{d}_s^n) - \hat{w}_s^n.$$

3.2. The RN partitioned FSI system

We replace two interface conditions in (4) by the following RN transmission conditions

$$\begin{aligned} \alpha_f u^{n+1} \circ \mathcal{A}^* + \sigma_f(u^{n+1}, p^{n+1}) n_f \circ \mathcal{A}^* = &\quad \alpha_f \delta_t \hat{d}_s^{n+1} - \hat{\sigma}_s(\hat{d}_s^{n+1}) \hat{n}_s \quad \text{on } \Gamma^0, \\ \hat{\sigma}_s(\hat{d}_s^{n+1}) \hat{n}_s = &\quad -\sigma_f(u^{n+1}, p^{n+1}) n_f \circ \mathcal{A}^* \quad \text{on } \Gamma^0, \end{aligned}$$

where $\alpha_f > 0$ is a Robin weighting parameter.

Then the RN partitioned iteration reads: Given u^n, $\hat{d}_s^n$, $\hat{w}_s^n$ and the current iteration $\hat{d}_s^k$, find u^{k+1}, p^{k+1} and $\hat{d}_s^{k+1}$ for the next iteration such that

$$\rho_f \delta_t u^{k+1}|_{x_0} + \rho_f((u^* - w_f^*) \cdot \nabla) u^{k+1} - \nabla \cdot \sigma_f(u^{k+1}, p^{k+1}) = 0 \quad \text{in } \Omega_f^*, \tag{6a}$$

$$\nabla \cdot u^{k+1} = 0 \quad \text{in } \Omega_f^*, \tag{6b}$$

$$\alpha_f u^{k+1} + \sigma_f(u^{k+1}, p^{k+1}) n_f = \alpha_f \delta_t \hat{d}_s^k \circ \mathcal{A}^{*-1} - \hat{\sigma}_s(\hat{d}_s^k) \hat{n}_s \circ \mathcal{A}^{*-1} \quad \text{on } \Gamma^*, \tag{6c}$$

and

$$\rho_s \delta_{tt} \hat{d}_s^{k+1} - \nabla \cdot \hat{\sigma}_s(\hat{d}_s^{k+1}) = 0 \quad \text{in } \Omega_s^0, \tag{7a}$$

$$\hat{\sigma}_s(\hat{d}_s^{k+1}) \hat{n}_s = -\sigma_f(u^{k+1}, p^{k+1}) n_f \circ \mathcal{A}^* \quad \text{on } \Gamma^0, \tag{7b}$$

where $\Gamma^* = \Gamma^0 \circ \mathcal{A}^{*-1}$, and k indicates the RN iteration level. Here for simplicity, we omit the super-index n for the time level t^n. It is easy to see those two interface conditions in (4) are fulfilled by iteratively applying (6c) and (7b) in the above partitioned iterations.

In the limit cases $\alpha_f = +\infty$ and $\alpha_f = 0$, the conventional DN and Neumann-Neumann (NN) preconditioned iterations are recovered, respectively, which show slow convergence in our FSI problem, see Section 6.

3.3. Weak formulations

Let $H^1(\Omega_s^0)$, $H^1(\Omega_f^0)$ and $L^2(\Omega_f^0)$ denote the standard Sobolev and Lebesgue spaces (see [1]) on Ω_s^0 and Ω_f^0, respectively. For the fluid, the function spaces for the velocity and pressure are respectively given by

$$V_f^*(t) = \{v_f | v_f = \hat{v}_f \circ \mathcal{A}^{*-1},\ \hat{v}_f \in [H^1(\Omega_f^0)]^3\},$$

$$Q_f^*(t) = \{q_f | q_f = \hat{q}_f \circ \mathcal{A}^{*-1},\ \hat{q}_f \in L^2(\Omega_f^0)\}.$$

For the structure, we define

$$\hat{V}_s = [H^1(\Omega_s^0)]^3 \text{ and } \hat{V}_s^0 = \{\hat{v}_s \in \hat{V}_s | \hat{v}_s = 0 \text{ on } \Gamma_d^0\},$$

where $\hat{V}_s^0$ is used for both trial and test function spaces due to the boundary condition (2g).

3.3.1. The weak formulation of the time discretized fluid problem

By the standard technique applied to the time discretized fluid subproblem (6), for a Robin iteration level $k+1$, we obtain the following mixed variational problem: Find $(u^{k+1}, p^{k+1}) \in V_f^*(t^{n+1}) \times Q_f^*(t^{n+1})$ such that

$$\begin{aligned} a_f(u^{k+1}, v_f) + b(v_f, p^{k+1}) &= \langle F_f^n, v_f \rangle, && \text{(8a)} \\ b(u^{k+1}, q_f) &= 0 && \text{(8b)} \end{aligned}$$

for all $v_f \in V_f^*(t^{n+1})$ and $q_f \in Q_f^*(t^{n+1})$, with the bilinear and linear forms

$$\begin{aligned} a_f(u, v_f) &= (\rho_f u/\Delta t, v_f)_{\Omega_f^*} + (\rho((u^* - w_f^*) \cdot \nabla)u, v_f)_{\Omega_f^*} \\ &\quad + (2\mu\varepsilon(u), \nabla v_f)_{\Omega_f^*} + (\alpha_f u, v_f)_{\Gamma^*} \\ b(v_f, q_f) &= -(q_f, \nabla \cdot v_f)_{\Omega_f^*} \\ \langle F_f^n, v_f \rangle &= (\rho_f u^n/\Delta t, v_f)_{\Omega_f^*} + \langle g_{in}, v_f \rangle_{\Gamma_{in}^*} + (\alpha_f(\hat{d}_s^k - \hat{d}_s^n) \circ \mathcal{A}^{*-1}/\Delta t, v_f)_{\Gamma^*} \\ &\quad - \langle \hat{\sigma}_s(\hat{d}_s^k)\hat{n}_s \circ \mathcal{A}^{*-1}, v_f \rangle_{\Gamma^*}, \end{aligned}$$

where $\Gamma_{in}^* = \Gamma_{in}^0 \circ \mathcal{A}^{*-1}$, $(\cdot,\cdot)_{\Omega_f^*}$ denotes the product in $L^2(\Omega_f^*) \times L^2(\Omega_f^*)$, $(\cdot,\cdot)_{\Gamma^*}$ the product in $H^{1/2}(\Gamma^*) \times H^{1/2}(\Gamma^*)$, and $\langle \cdot,\cdot \rangle_{\Gamma^*}$ the duality product in $H^{1/2}(\Gamma^*) \times H^{-1/2}(\Gamma^*)$. Here $H^{1/2}(\Gamma^*)$ denotes the Sobolev space of the trace on Γ^* of functions from $V_f^*(t)$, and $H^{-1/2}(\Gamma^*)$ its dual.

3.3.2. The weak formulation of the time discretized structure problem

For the displacement of the structure sub-problem (7) on a Neumann iteration level $k+1$ for the time level t^{n+1}, the following variational problem must be solved: Find $\hat{d}_s^{k+1} \in \hat{V}_s^0$ such that

$$a_s(\hat{d}_s^{k+1}, \hat{v}_s) = \langle \hat{F}_s^n, \hat{v}_s \rangle \tag{9}$$

for all $\hat{v}_s \in \hat{V}_s^0$, with the bilinear and linear forms

$$a_s(\hat{d}_s, \hat{v}_s) = (2\rho_s \hat{d}_s/\Delta t^2, \hat{v}_s)_{\Omega_s^0} + (\lambda^l \nabla \cdot \hat{d}_s, \nabla \cdot \hat{v}_s)_{\Omega_s^0} + (2\mu^l \varepsilon(\hat{d}_s), \nabla \hat{v}_s)_{\Omega_s^0},$$
$$\langle \hat{F}_s^n, \hat{v}_s \rangle = (2\rho_s(\hat{d}_s^n + \Delta t \hat{w}_s^n)/\Delta t, \hat{v}_s)_{\Omega_s^0} - \langle \sigma_f(u^{k+1}, p^{k+1}) n_f \circ \mathcal{A}^*, \hat{v}_s \rangle_{\Gamma_0},$$

where $(\cdot,\cdot)_{\Omega_s^0}$ denotes the product in $L^2(\Omega_s^0) \times L^2(\Omega_s^0)$, $\langle \cdot, \cdot \rangle_{\Gamma^0}$ the duality product in $H^{1/2}(\Gamma^0) \times H^{-1/2}(\Gamma^0)$.

Note that on the interface we impose a conformity of traces of functions from the fluid velocity and structure displacement spaces, i.e.,

$$v_f \circ \mathcal{A}^* = \hat{v}_s \text{ on } \Gamma^0$$

for $v_f \in V_f^*(t)$ and $\hat{v}_s \in \hat{V}_s^0$.

3.4. Finite element discretization on a hybrid mesh

The spatial discretization was done by a finite element method on the underlying hybrid mesh composed of four types of elements: tetrahedra, hexahedra, pyramids and prisms. We briefly describe the extension of the standard P_1 element on pure tetrahedral meshes to hybrid meshes.

Let $\mathcal{M}_h$ be an admissible triangulation of a computational domain Ω into polyhedral elements. For each non-tetrahedral element M, a subdivision into a number of tetrahedra is performed in the following way: we subdivide each non-triangular face into triangles by connecting an introduced center node of the face with all original vertices on that face. Then we add another node at the center of M and connect this node with all vertices and all face centers. By this means, a prism is split into 14 tetrahedra, a hexahedra into 24 tetrahedra, and a pyramid into 8 tetrahedra, see Fig. 2 for an illustration. One easily sees that such a subdivision results in an admissible refinement $\mathcal{T}_h$ of the original hybrid mesh $\mathcal{M}_h$.

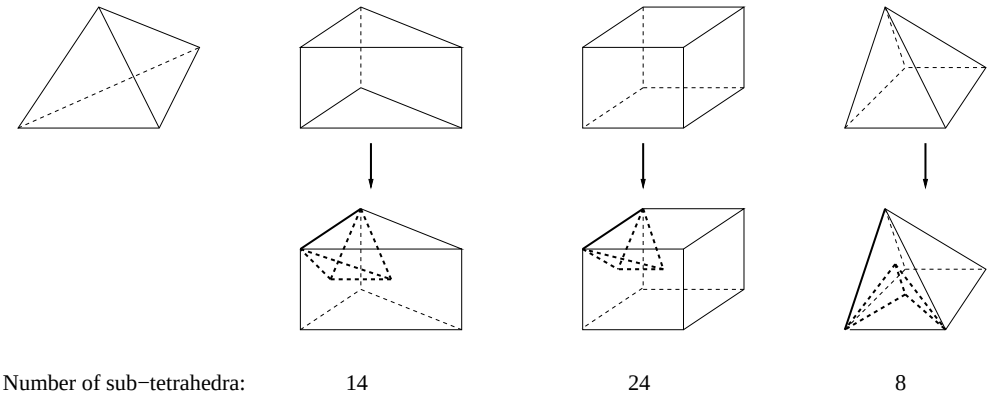

Figure 2: Splitting of element domains into tetrahedra.

3.4.1. The extended P_1 element on a hybrid mesh

For constructing the extended P_1 element on $\mathcal{M}_h$, we firstly consider a nodal basis function on an element M from $\mathcal{M}_h$ as follows: Let x be a vertex of M, let x_{F_i}, $i = 1, ...,$ denote the center of those non-triangular faces F_i which contain x as a vertex, and let x_M denote the center of M. Then on the element M, the nodal basis function φ associated with the vertex x is given by

$$\varphi = \hat{\varphi} + \sum_i \frac{1}{N_{F_i}} \hat{\varphi}_{F_i} + \frac{1}{N_M} \hat{\varphi}_M \ , \tag{10}$$

where $\hat{\varphi}$, $\hat{\varphi}_{F_i}$, and $\hat{\varphi}_M$ denote the nodal basis functions of the P_1 element on the subdivision of M associated with the nodes x, x_{F_i} and x_M, respectively, and N_{F_i} and N_M are the numbers of vertices of the face F_i and the element M, respectively. Note that in case of pure tetrahedral meshes, we have $\varphi = \hat{\varphi}$. The numerical solutions of the FSI problem on hybrid and pure tetrahedral meshes are compared with each other in Section 6.

Then the finite element space of the extended P_1 element on $\mathcal{M}_h$ is constructed by a span of the local basis functions on each element M, i.e.,

$$V_h = \{v \in C(\overline{\Omega}) : v|_M \in \Phi_M, \forall M \in \mathcal{M}_h\}, \tag{11}$$

where

$$\Phi_M = \text{span}\{\varphi : M \in \mathcal{M}_h\}.$$

One easily sees that the extended P_1 element is an $H^1(\Omega)$-conforming finite element and the following approximation properties as the standard P_1

element on tetrahedral meshes hold:

Theorem 1 ([28]). 1. *There is an interpolation operator* $I_C\colon L^2(\Omega) \longrightarrow V_h$ *such that*

$$\|v - I_C v\|_{L^2(\Omega)} \leq c\,|v|_{L^2(\Omega)} \quad \textit{for all } v \in L^2(\Omega),$$

and

$$\|v - I_C v\|_{L^2(\Omega)} + h|v - I_C v|_{H^1(\Omega)} \leq c\,h\,|v|_{H^1(\Omega)} \quad \textit{for all } v \in H^1(\Omega)$$

with a mesh-independent constant c.

2. *There is an interpolation operator* $I_L\colon H^2(\Omega) \longrightarrow V_h$ *such that*

$$\|v - I_L v\|_{L^2(\Omega)} + h|v - I_L v|_{H^1(\Omega)} \leq c\,h^2\,|v|_{H^2(\Omega)} \quad \textit{for all } v \in H^1(\Omega)$$

with a mesh-independent constant c.

The operators I_C and I_L are the Clément-type interpolation operator and the Lagrange-type interpolation operator, respectively. For details, see [25].

Note that the constructed nodal basis function φ has a larger support compared to that for the standard P_1 element, see Fig. 3 for an illustration. However, the degrees of freedom for the extended P_1 element are only associated with the vertices from $\mathcal{M}_h$. Therefore it has fewer degrees of freedom compared to that for the standard P_1 element.

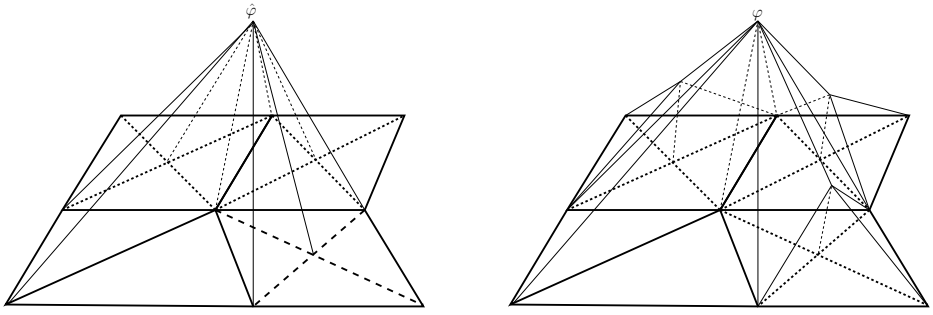

(a) Standard P_1 on $\mathcal{T}_h$ (b) Extended P_1 on $\mathcal{M}_h$

Figure 3: A schematic representation of a nodal basis function for the standard P_1 element on subdivisions (indicated by thick dashed lines) of non-triangle elements (left) and for the extended P_1 element on hybrid elements (right).

3.4.2. The extended P_1 element for the structure sub-problem

In the FSI problem, we assume that the computational domains Ω_s^0 and Ω_f^0 are triangulated by a hybrid mesh with matching vertices on the interface Γ^0.

By specifying the domain $\Omega = \Omega_s^0$ in (11) we obtain the extended P_1 element space $\hat{V}_{s,h} = [V_h]^3$ for the displacement. Then the fully discretized structure problem for a RN iteration $k+1$ reads: Find $\hat{d}_{s,h}^{k+1} = \hat{V}_{s,h} \cap \hat{V}_s^0$ such that

$$a_{s,h}(\hat{d}_{s,h}^{k+1}, \hat{v}_{s,h}) = \langle \hat{F}_{s,h}^n, \hat{v}_{s,h} \rangle \tag{12}$$

for all $\hat{v}_{s,h} = \hat{V}_{s,h} \cap \hat{V}_s^0$, with the bilinear and linear forms

$$a_{s,h}(\hat{d}_{s,h}^{k+1}, \hat{v}_{s,h}) = a_s(\hat{d}_{s,h}^{k+1}, \hat{v}_{s,h}),$$
$$\langle \hat{F}_{s,h}^n, \hat{v}_{s,h} \rangle = (2\rho_s(\hat{d}_{s,h}^n + \Delta t \hat{w}_{s,h}^n)/\Delta t, \hat{v}_{s,h})_{\Omega_s^0} - \langle \sigma_f(u_h^{k+1}, p_h^{k+1}) n_f \circ \mathcal{A}^*, \hat{v}_{s,h} \rangle_{\Gamma_0},$$

where $\hat{d}_{s,h}^n$ is the finite element approximation of the structure displacement on time level t^n, $\hat{w}_{s,h}^n$ denotes the approximation of the structure velocity on time level t^n, u_h^{k+1} and p_h^{k+1} are the finite element approximations of the fluid velocity and pressure on a RN iteration $k+1$ on time level t^{n+1}.

3.4.3. The stabilized and extended P_1 element for the fluid sub-problem

The hybrid mesh for Ω_f^* is obtained by moving the vertices of the hybrid mesh for Ω_f^0 with the displacement $\hat{d}_{f,h}^n$. The displacement $\hat{d}_{f,h}^n$ is calculated by solving the discretized problem for the harmonic extension (1) in $D_{f,h} = \{\hat{d} \in [V_h]^3 : \hat{d} = 0 \text{ on } \Gamma_{in}^0 \cup \Gamma_{out}^0\}$: Find $\hat{d}_{f,h} \in \{\hat{d} \in D_{f,h} : \hat{d} = \hat{d}_{s,h}^n \text{ on } \Gamma^0\}$ such that

$$\int_{\Omega_f^0} \nabla \hat{d}_{f,h} : \nabla \hat{v}_{f,h} d\Omega_f^0 = 0$$

for all $\hat{v}_{f,h} \in \{\hat{v} \in D_{f,h} : \hat{v} = 0 \text{ on } \Gamma^0\}$, where V_h is obtained by specifying the domain $\Omega = \Omega_f^0$ in (11).

Then we construct the finite element spaces

$$V_{f,h}^*(t^{n+1}) = [V_h]^3 \text{ and } Q_{f,h}^*(t^{n+1}) = V_h$$

for the velocity and pressure, respectively, where V_h is obtained by using the hybrid mesh for Ω_f^* in (11).

As is well known, the equal order approximations for both velocity and pressure usually suffer a violation of the discrete $\inf - \sup$ condition. In

addition, an instability may be caused by a dominating convection term. See [6, 14] for details. For resolving these two problems, we adopt the same stabilization terms for linear elements as in [12], which are applied to the tetrahedral refinement of the original hybrid mesh.

The fully discretized and stabilized fluid problem for a RN iteration $k+1$ reads: Find $(u_h^{k+1}, p_h^{k+1}) \in V_{f,h}^*(t^{n+1}) \times Q_{f,h}^*(t^{n+1})$ such that

$$\begin{aligned} a_{f,h}(u_h^{k+1}, v_{f,h}) + b_{1,h}(v_{f,h}, p_h^{k+1}) &= \langle F_{f,h}^n, v_{f,h} \rangle, & \text{(13a)} \\ b_{2,h}(u_h^{k+1}, q_h) - c_{f,h}(p_h^{k+1}, q_h) &= \langle G_{f,h}^n, q_h \rangle, & \text{(13b)} \end{aligned}$$

for all $v_{f,h} \in V_{f,h}^*(t^{n+1})$ and $q_h \in Q_{f,h}^*(t^{n+1})$, with the bilinear and linear forms

$$\begin{aligned} a_{f,h}(u_h^{k+1}, v_{f,h}) &= a_f(u_h^{k+1}, v_{f,h}) \\ &\quad - \sum_{M \in \mathcal{M}_h} \sum_{T \subset M} \frac{\tau_T}{\Delta t}(u_h^{k+1} + \Delta t(u_h^* - w_{f,h}^*) \cdot \nabla u_h^{k+1}, r_T v_{f,h} - \Delta t(u_h^* - w_{f,h}^*) \cdot \nabla v_{f,h}) \\ &\quad + \sum_{M \in \mathcal{M}_h} \sum_{T \subset M} \frac{\gamma_T}{\Delta t}(\nabla \cdot (u_h^{k+1}, \nabla \cdot v_{f,h}), \end{aligned}$$

$$\begin{aligned} b_{1,h}(\nabla p_h^{k+1}, v_{f,h}) &= b_f(\nabla p_h^{k+1}, v_{f,h}) \\ &\quad - \sum_{M \in \mathcal{M}_h} \sum_{T \subset M} \tau_T(\nabla p_h^{k+1}, r_T v_{f,h} - \Delta t(u_h^* - w_{f,h}^*) \cdot \nabla v_{f,h}), \end{aligned}$$

$$b_{2,h}(u_h^{k+1}, \nabla q_h) = b_f(u_h^{k+1}, \nabla q_h) - \sum_{M \in \mathcal{M}_h} \sum_{T \subset M} \tau_T(u_h^{k+1} + \Delta t(u_h^* - w_{f,h}^*) \cdot \nabla u_h^{k+1}, \nabla q_h),$$

$$c_{f,h}(\nabla p_h^{k+1}, \nabla q_h) = \sum_{M \in \mathcal{M}_h} \sum_{T \subset M} \tau_T(\nabla p_h^{k+1}, \Delta t \nabla q_h),$$

$$\langle F_{f,h}^n, v_{f,h} \rangle = \langle F_f^n, v_f \rangle - \sum_{M \in \mathcal{M}_h} \sum_{T \subset M} \frac{\tau_T}{\Delta t}(u_h^n, r_T v_{f,h} - \Delta t(u_h^* - w_{f,h}^*) \cdot \nabla v_{f,h}),$$

$$\langle G_{f,h}^n, q_h \rangle = - \sum_{M \in \mathcal{M}_h} \sum_{T \subset M} \tau_T(u_h^n, \nabla q_h)$$

with the finite element approximations u_h^*, w_h^* and u_h^n for u^*, w^* and u^n, respectively. Here the third terms in $a_{f,h}(\cdot,\cdot)$ provides an additional stability at high Reynolds numbers. We refer to [13, 7, 19] for details. The stabilization

parameters are give by

$$
\begin{aligned}
r_T &= \min(1 - \Delta t \nabla(u_h^* - w_h^*), 1), \\
\tau_T &= \min\left(\frac{h_T^2}{h_T^2 \xi_1 + 12\Delta t \mu \xi_2}, \sigma_{0T}\right), \\
\gamma_T &= \Delta t \sqrt{4\mu^2 + 4h_T^2 |u_h^* - w_h^*|^2},
\end{aligned}
$$

where h_T is the mesh parameter of T,

$$
\xi_1 = \max(\frac{12\Delta t \mu}{h_T^2}, 1), \quad \xi_2 = \max(\frac{h_T |u_h^* - w_h^*|}{6\mu}, 1),
$$

$$
\sigma_{0T} = \begin{cases} 1 & \text{if } \nabla \cdot (u_h^* - w_h^*) \leq 0, \\ 1 - \frac{\Delta t}{2}(\nabla \cdot (u_h^* - w_h^*)) & \text{if } \nabla \cdot (u_h^* - w_h^*) > 0. \end{cases}
$$

3.4.4. Linear systems for the structure and fluid sub-problems

After the linearization, the temporal and spatial discretization, two linear systems for sub-problems (6)-(7) arise for each RN iteration $k+1$ for the time level t^{n+1}. The following ansatz

$$
\hat{d}_{s,h}^{k+1} = \sum_{j=1}^{n_s} d_j \varphi_j, \; u_h^{k+1} = \sum_{j=1}^{n_f} u_j \varphi_j \text{ and } p_h^{k+1} = \sum_{j=1}^{n_f} p_j \varphi_j
$$

for the structure displacement, and the fluid velocity and pressure are used in (12) and (13), respectively. Here $d_j \in \mathbb{R}^3$, $u_j \in \mathbb{R}^3$, $p_j \in \mathbb{R}$, n_s and n_f denote the number of vertices from the structure and fluid meshes, respectively, and the nodal basis function φ_j for each corresponding variable has a form of (10). This gives rise to the following two linear systems of equations:

$$
A_s \underline{d}_s = \underline{f}_s \text{ and } K_f \begin{pmatrix} \underline{u} \\ \underline{p} \end{pmatrix} = \begin{pmatrix} \underline{f}_f \\ \underline{g} \end{pmatrix}, \tag{14}
$$

a symmetric and positive definite (SPD) system for the structure sub-problem, and a saddle point system for the fluid sub-problem, respectively. Here $K_f = \begin{pmatrix} A_f & B_1^T \\ B_2 & -C_f \end{pmatrix}$, $\underline{d}_s = (d_i)$, $\underline{u}_f = (u_i)$ and $\underline{p}_f = (p_i)$. We refer to [25] for the finite element assembly of the matrices and the right hand side vectors. The special algebraic multigrid solvers for these two linear systems of equations in (14) will be discussed in Section 5.

4. The RN preconditioned method in an algebraic form

In this section, we reinterpret the RN iterations (6)-(7) in an algebraic form. For this, we first permute the linear systems of equations in (14) according to the splittings of the degrees of freedom associated with the interface vertices and the remaining ones.

The reordered linear system for the structure problem reads:

$$\mathcal{X}\begin{pmatrix} D_\Gamma \\ D_s \end{pmatrix} = \begin{pmatrix} F_{s\Gamma} \\ F_s \end{pmatrix} \text{ with } \mathcal{X} = \begin{pmatrix} X_{\Gamma\Gamma} & X_{\Gamma s} \\ X_{s\Gamma} & X_{ss} \end{pmatrix}, \tag{15}$$

a permuted stiffness matrix of A_s. Here the block diagonal matrices $X_{\Gamma\Gamma}$ and X_{ss} represent the stiffness matrices assembled from the degrees of freedom associated with the interface vertices and the remaining ones, respectively, and the off-diagonal matrices $X_{s\Gamma}$ and $X_{\Gamma s}$ are assembled from the coupling of degrees of freedom associated with the interface vertices and its connected remaining ones.

In an analogous way, the reordered linear system for the fluid problem reads:

$$\mathcal{Y}\begin{pmatrix} V_f \\ V_\Gamma \end{pmatrix} = \begin{pmatrix} F_f \\ F_{f\Gamma} \end{pmatrix} \text{ with } \mathcal{Y} = \begin{pmatrix} Y_{ff} & Y_{f\Gamma} \\ Y_{\Gamma f} & Y_{\Gamma\Gamma} \end{pmatrix} + \begin{pmatrix} 0 & 0 \\ 0 & \alpha_f M_\Gamma \end{pmatrix}, \tag{16}$$

a permuted matrix of K_f. Here the block diagonal matrices $Y_{\Gamma\Gamma}$ and Y_{ff} are assembled from the velocity degrees of freedom associated with the interface vertices and all the other degrees of freedom associated with the corresponding vertices, respectively

4.1. The Schur complement equation

Recall we aim at solving the linearized FSI system (4) on each time level. Using the notations introduced in the permuted systems (15)-(16), the finite element discretization of the coupled system gives rise to the following system

$$\begin{pmatrix} Y_{ff} & Y_{f\Gamma} & 0 & 0 \\ 0 & M_\Gamma & -M_\Gamma/\Delta t & 0 \\ Y_{\Gamma f} & Y_{\Gamma\Gamma} & X_{\Gamma\Gamma} & X_{\Gamma s} \\ 0 & 0 & X_{s\Gamma} & X_{ss} \end{pmatrix} \begin{pmatrix} V_f \\ V_\Gamma \\ D_\Gamma \\ D_s \end{pmatrix} = \begin{pmatrix} F_f \\ -M_\Gamma/\Delta t D_\Gamma^n \\ F_\Gamma \\ F_s \end{pmatrix}. \tag{17}$$

Here F_Γ corresponds to the sum of two contributions from $F_{s\Gamma}$ and $F_{f\Gamma}$, without including the Robin boundary condition part in $F_{f\Gamma}$, and M_Γ is the interface mass matrix given by $M_\Gamma = (\varphi, \varphi)_{\Gamma^*} I$.

The Schur complement equation for (17) reads:

$$\mathcal{S}_\Gamma D_\Gamma = H_\Gamma \tag{18}$$

where

$$\mathcal{S}_\Gamma = \underbrace{X_{\Gamma\Gamma} - X_{\Gamma s}X_{ss}^{-1}X_{s\Gamma}}_{:=\tilde{X}_\Gamma} + \underbrace{Y_{\Gamma\Gamma}/\Delta t - Y_{\Gamma f}Y_{ff}^{-1}Y_{f\Gamma}/\Delta t}_{:=\tilde{Y}_\Gamma},$$

and the right hand side is given by

$$H_\Gamma = F_\Gamma - Y_{\Gamma f}Y_{ff}^{-1}(F_f + Y_{f\Gamma}D_\Gamma^n/\Delta t) + Y_{\Gamma\Gamma}D_\Gamma^n/\Delta t - X_{\Gamma s}X_{ss}^{-1}F_s. \tag{19}$$

Here we reformulate a Schur complement equation in terms of the structure displacement unknowns, which keeps the modularity of the code developed [25, 28].

4.2. The RN iteration in an algebraic form

One easily sees that each RN iteration is able to be reformulated in an algebraic form: Given D_Γ^k and the solutions from the previous time step, find D_Γ^{k+1} such that the following equations

$$\begin{aligned}
X_{ss}\tilde{D}_s^{k+1} &= F_s - X_{s\Gamma}D_\Gamma^k, \\
\mathcal{Y}\begin{pmatrix} V_f^{k+1} \\ V_\Gamma^{k+1} \end{pmatrix} &= \begin{pmatrix} F_f \\ F_\Gamma \end{pmatrix} - \begin{pmatrix} 0 \\ X_{\Gamma s}\tilde{D}_s^{k+1} + (X_{\Gamma\Gamma} - \alpha_f M_\Gamma/\Delta t)D_\Gamma^k + \alpha_f M_\Gamma D_\Gamma^n/\Delta t \end{pmatrix}, \\
\mathcal{X}\begin{pmatrix} D_\Gamma^{k+1} \\ D_s^{k+1} \end{pmatrix} &= \begin{pmatrix} F_\Gamma \\ F_s \end{pmatrix} - \begin{pmatrix} Y_{\Gamma f}V_f^{k+1} + Y_{\Gamma\Gamma}V_\Gamma^{k+1} \\ 0 \end{pmatrix}
\end{aligned}$$

are fulfilled, where the first one corresponds to a structure problem with a prescribed Dirichlet boundary condition D_Γ^k on the interface. After an elementary algebraic manipulation of the above three equations, we obtain a preconditioned Richardson iteration applied to the Schur complement equation (18):

$$D_\Gamma^{k+1} = D_\Gamma^k + P_\Gamma^{-1}(H_\Gamma - \mathcal{S}_\Gamma D_\Gamma^k), \tag{21}$$

where the preconditioner P_Γ is formulated in the following way

$$P_\Gamma = \left(\frac{\Delta t}{\alpha_f}\tilde{Y}_\Gamma + M_\Gamma\right) M_\Gamma^{-1}\tilde{X}_\Gamma. \tag{22}$$

The iterative process needs to be supplemented with an appropriate stopping criterion, e.g., a relative error reduction

$$\|D_\Gamma^{k+1} - D_\Gamma^k\|/\|D_\Gamma^0\| \le \varepsilon \tag{23}$$

is used in the numerical experiments.

4.3. The RN preconditioned GMRES solver

The preconditioned Richardson iteration (21) on the Schur complement equations is accelerated by the GMRES solver. For this, we need to generate the Krylov basis associated with the matrix $Q = P_\Gamma^{-1}\mathcal{S}_\Gamma$. The generated Krylov space at the m-th iteration is

$$\mathcal{K}_m := \text{span}\{r^0, Qr^0, Q^2r^0, .., Q^{m-1}r^0\} = \text{span}\{z^0, z^1, ..., z^{m-1}\},$$

where $r^0 = P_\Gamma^{-1}(H_\Gamma - \mathcal{S}_\Gamma D_\Gamma^0)$ is obtained by applying a preconditioned Richardson iteration with an initial guess D_Γ^0. Here $\{z^k\}$ is an orthonormal basis in the GMRES, which is obtained in the following: Given z^k, we evaluate a matrix-vector product $w = P_\Gamma^{-1}\mathcal{S}_\Gamma z^k$ and then $z^{k+1} = w - \Pi_{\mathcal{K}_m} w$, where $\Pi_{\mathcal{K}_m}$ is an orthogonal projection operator onto $\mathcal{K}_m$.

The product w is given by $w = z^k - d_\Gamma$ with $d_\Gamma = z^k - P_\Gamma^{-1}\mathcal{S}_\Gamma z^k$, which is obtained by applying a preconditioned Richardson iteration (with enforced $H_\Gamma = 0$ of (19)): Given z^k, find d_Γ such that

$$\begin{aligned} X_{ss}\tilde{d}_s &= -X_{s\Gamma}z^k, && \text{(24a)}\\ \mathcal{Y}\begin{pmatrix} v_f \\ v_\Gamma \end{pmatrix} &= -\begin{pmatrix} 0 \\ X_{\Gamma s}\tilde{d}_s + (X_{\Gamma\Gamma} - \alpha_f M_\Gamma/\Delta t)z^k \end{pmatrix}, && \text{(24b)}\\ \mathcal{X}\begin{pmatrix} d_\Gamma \\ d_s \end{pmatrix} &= -\begin{pmatrix} Y_{\Gamma f}v_f + Y_{\Gamma\Gamma}v_\Gamma \\ 0 \end{pmatrix}. && \text{(24c)} \end{aligned}$$

In fact, from the above three steps, it is easy to calculate

$$d_\Gamma = \Delta t\tilde{X}_\Gamma^{-1}\tilde{Y}_\Gamma(\Delta t\tilde{Y}_\Gamma + \alpha_f M_\Gamma)^{-1}(\tilde{X}_\Gamma - \alpha_f M_\Gamma/\Delta t)z^k.$$

Hence, we have

$$z^k - d_\Gamma = (I - \Delta t\tilde{X}_\Gamma^{-1}\tilde{Y}_\Gamma(\Delta t\tilde{Y}_\Gamma + \alpha_f M_\Gamma)^{-1}(\tilde{X}_\Gamma - \alpha_f M_\Gamma/\Delta t))z^k = P_\Gamma^{-1}\mathcal{S}_\Gamma z^k.$$

5. AMG methods for the structure and fluid sub-problems

The remaining task is concerned with special AMG methods for solving two linear systems of equations in (14).

For the structure problem, since the variational problem on the structure domain is symmetric and coercive this leads to linear systems with SPD matrices. AMG methods for solving such problems are well-studied, see, e.g., [20] for scalar differential equations and [15] for an extension to systems

of partial differential equations in a natural blockwise fashion (blockwise interpolation). The special AMG method used in our experiments is taken from the work of [16], which was originally developed for discrete elliptic second-order problems and was extended to the structure problem on hybrid meshes in a straightforward way, see [28, 25].

5.1. The AMG method for the fluid problem

For the fluid problem in (14), special care has to be taken into account since the matrix in the linear system is not coercive. The standard Galerkin projection for generating a hierarchy of linear systems derived from the original discretized system by some coarsening strategy does not necessarily inherit the stability property due to a possible violation of the discrete $\inf - \sup$ condition. For curing this, based on the work by Markus Wabro (see [22, 23, 24]), we extended the stabilized coarsening strategy to the discretized fluid problems on hybrid meshes. For simplicity we present the idea for the Stokes problem only. The extension of the technique to more general fluid sub-problems arising in the FSI problem is detailed in [25].

The saddle point problem arising from the stabilized discretization of the Stokes problem using the extended P_1 element is given by

$$K \begin{pmatrix} u \\ p \end{pmatrix} = \begin{pmatrix} f \\ g \end{pmatrix} \tag{25}$$

with $K = \begin{pmatrix} A & B^T \\ B & -C \end{pmatrix}$ obtained by only keeping the pressure stabilization term $c_{f,h}(\cdot,\cdot)$ in (13), where A is SPD, B has full rank, and C is symmetric and positive semi-definite. One easily sees that the (negative) Schur complement

$$S = BA^{-1}B^T + C$$

is SPD.

The AMG method requires an appropriate coarsening strategy and a smoothing procedure.

5.1.1. The stabilized coarsening strategy

For avoiding a mixture of the velocity and pressure unknowns on coarse levels, we construct the prolongation operator from the coarse level $l+1$ to the next finer level l in a block-diagonal matrix form:

$$P_{l+1}^l : \begin{pmatrix} (\mathbb{R}^3)^{m_{l+1}} \\ \mathbb{R}^{m_{l+1}} \end{pmatrix} \longrightarrow \begin{pmatrix} (\mathbb{R}^3)^{m_l} \\ \mathbb{R}^{m_l} \end{pmatrix}, \quad P_{l+1}^l = \begin{pmatrix} I_{l+1}^l & \\ & J_{l+1}^l \end{pmatrix}, \tag{26}$$

where m_l is the number of velocity (pressure) degrees of freedom on the level l, I_{l+1}^l and J_{l+1}^l are prolongation matrices for the velocity and pressure, respectively.

For the restriction from the finer level l to the next coarser level $l+1$ we choose the transposed matrix:

$$R_l^{l+1} = (P_{l+1}^l)^T = \begin{pmatrix} I_l^{l+1} & \\ & J_l^{l+1} \end{pmatrix},$$

where $I_l^{l+1} = (I_{l+1}^l)^T$ and $J_l^{l+1} = (J_{l+1}^l)^T$. The system matrix on the level l is denoted by K_l with a form

$$K_l = \begin{pmatrix} A_l & B_l^T \\ B_l & -C_l \end{pmatrix}.$$

The system matrix on the next coarser level $l+1$ is obtained by the Galerkin projection method:

$$K_{l+1} = R_l^{l+1} K_l P_{l+1}^l = \begin{pmatrix} A_{l+1} & B_{l+1}^T \\ B_{l+1} & -C_{l+1} \end{pmatrix}$$

with $A_{l+1} = I_l^{l+1} A_l I_{l+1}^l$, $B_{l+1} = J_l^{l+1} B_l I_{l+1}^l$, $C_{l+1} = J_l^{l+1} C_l J_{l+1}^l$.

Since the matrix C involves mesh-dependent stabilization parameters, the Galerkin projection for C_{l+1} may cause a loss of stability on coarser levels. Therefore a remedy is applied for coarsening C: we set

$$C_{l+1} = \frac{1}{h^2} \lambda_{\max}(D_l^{-1} M_l) \tilde{C}_{l+1},$$

where $\tilde{C}_{l+1}$ denotes the standard Galerkin projection of C, h the mesh parameter on the finest level, M_l is the mass matrix on level l obtained by Galerkin projection, D_l the diagonal of A_l.

Under appropriate assumptions on the hybrid mesh the following stability result was shown, see [25] for details:

Theorem 2. *For each level l, there is a constant $\zeta_l > 0$ such that*

$$\sup_{0 \neq (v,q) \in V_l \times Q_l} \frac{\mathcal{B}_l((u,p),(v,q))}{\|v\|_{A_l} + \|q\|_{M_l}} \geq \zeta_l \left(\|u\|_{A_l} + \|p\|_{M_l} \right)$$

for all $(u,p) \in V_l \times Q_l = (\mathbb{R}^3)^{m_l} \times \mathbb{R}^{m_l}$, where

$$\mathcal{B}_l((u,p),(v,q)) = v^T A_l u + v^T B_l^T p + q^T B_l u - q^T C_l p.$$

5.1.2. The smoothing procedure

A Braess-Sarazin-type smoother was used as the smoothing procedure, which was originally introduced in [5] and has a smoothing property with a rate of $\mathcal{O}(1/m)$, where m is the number of smoothing steps.

One step of the smoothing procedure consists of applications of the inexact Uzawa algorithm:

$$\begin{aligned}\hat{A}\,(\hat{u}^{k+1}-u^k) &= f - Au^k - B^T p^k,\\ \hat{S}\,(p^{k+1}-p^k) &= B\hat{u}^{k+1} - Cp^k - g,\\ \hat{A}\,(u^{k+1}-u^k) &= -B^T(p^{k+1}-p^k),\end{aligned}$$

which correspond to a preconditioned Richardson method:

$$\begin{pmatrix}u^{k+1}\\ p^{k+1}\end{pmatrix} = \begin{pmatrix}u^k\\ p^k\end{pmatrix} + \hat{K}^{-1}\begin{pmatrix}f - Au^k - B^T p^k\\ g - Bu^k + Cp^k\end{pmatrix}$$

with a symmetric and indefinite preconditioner

$$\hat{K} = \begin{pmatrix}\hat{A} & B^T\\ B & \hat{A}^{-1}B^T - \hat{S}\end{pmatrix},$$

where $\hat{A}$ and $\hat{S}$ are SPD preconditioners for A and the (negative) inexact Schur complement $C + B\hat{A}^{-1}B^T$, respectively.

As suggested in [22], we use $\hat{A} = 2D$ (a damped Jacobi iteration), where D denotes the diagonal of A. The choice $\hat{S} = C + B^T\hat{A}^{-1}B$ corresponds to the original Braess-Sarazin smoother. It requires the (exact) solution of the equation

$$(C + B^T\hat{A}^{-1}B)(p^{k+1} - p^k) = B\hat{u}^{k+1} - Cp^k - g.$$

We use instead one step of an (inner) AMG method with starting value 0 to solve this equation approximately. See [29] for an analysis of such an approximate Braess-Sarazin smoother.

6. Numerical experimentations

6.1. The RN preconditioned GMRES algorithm

For convenience of reading, we first summarize the RN preconditioned GMRES algorithm in Algorithm 1 for a schematic description of the computational method.

In our numerical experiments, we set the stopping threshold $\varepsilon = 10^{-5}$ in (23) for the GMRES iterations. For the inner AMG-PCG and AMG solvers, we set relative residual errors 10^{-2} as stopping criteria.

Algorithm 1 The RN preconditioned GMRES algorithm

1: **for** each time step $n = 1, ..., N$ **do**
2: **while** $\|D_\Gamma^{k+1} - D_\Gamma^k\|/\|D_\Gamma^0\| > \varepsilon$ **do**
3: apply the AMG-preconditioned conjugate gradient (AMG-PCG) solver to the structure sub-problem with the Dirichlet boundary condition (structure-Dirichlet) on the interface corresponding to (24a)
4: apply the AMG solver to the fluid sub-problem with the Robin boundary condition (fluid-Robin) on the interface corresponding to (24b)
5: apply the AMG-PCG solver to the structure sub-problem with the Neumann boundary condition (structure-Neumann) on the interface corresponding to (24c)
6: **end while**
7: **end for**

6.2. The setup of a numerical example

All the following numerical experiments are performed on a straight cylinder vessel, which is quite often used, see e.g., [28, 9]. The fluid domain is a cylinder in the z-direction of length 50 mm and radius 5 mm. The thickness of the surrounding structure is 1 mm.

Hybrid meshes[2] are generated for the fluid and the structure domains with matching vertices at the common interface. Two meshes are used for simulations, see Fig. 4. The coarse mesh contains $4,176$ vertices and $3,965$ elements ($1,944$ structure elements and $2,021$ fluid elements), and the fine mesh contains $17,904$ vertices and $17,489$ elements ($7,434$ structure elements and $10,055$ fluid elements). The overall degrees of freedom for these two meshes are about $16,000$ and $70,000$, respectively.

The structure medium is a linear Saint Venant-Kirchhoff material with the density $\rho^s = 1.2$ g/cm^3 and Lamé constants $\mu^l = 1.15 \times 10^6$ dyn/cm^2 and $\lambda^l = 1.73 \times 10^6$ dyn/cm^2. The fluid medium has the density $\rho^{\mathrm{f}} = 1.0$ g/cm^3 and the viscosity $\mu = 0.03$ poise. For the fluid, we set the Neumann data $g_{in} = (0, 0, 1.332 \times 10^4)^T$ dyn/cm^2 on the inlet for time $t \leq 3$ ms and $g_{in} = 0$ afterwards.

The structure and the fluid are initially at rest.

[2] [F.Kickinger, http://www.meshing.org/]

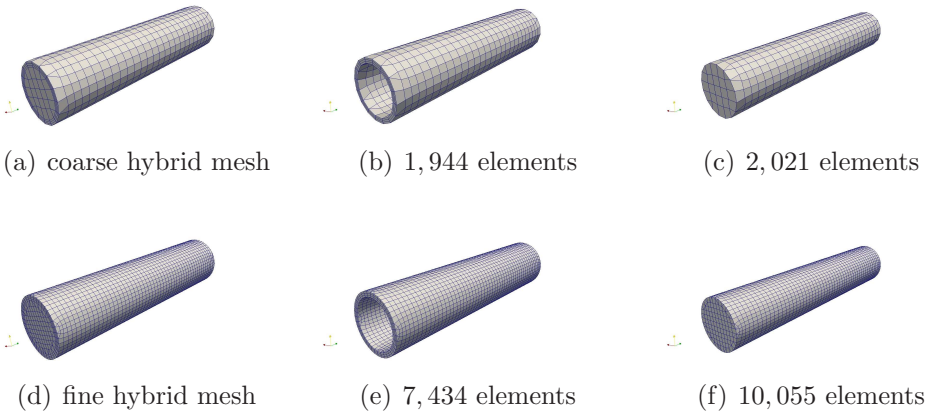

(a) coarse hybrid mesh (b) 1,944 elements (c) 2,021 elements

(d) fine hybrid mesh (e) 7,434 elements (f) 10,055 elements

Figure 4: Two meshes for the FSI computational domain: Coarse mesh (first row) and fine mesh (second row).

6.3. A comparison with the Newton based FSI Solver

The Newton based FSI solver on hybrid meshes was developed in the work of [25, 28, 27]. For convenience of a comparison with the RN preconditioned GMRES solver, we summarize it in Algorithm 2.

We set a relative error reduction 10^{-5} for the residual $-(S_s(\lambda^k)+S_f(\lambda^k))$ of the nonlinear interface equation. The evaluation of $S_s(\lambda^k)$ and $S_f(\lambda^k)$ requires to apply the AMG-PCG and AMG solvers to the structure and fluid sub-problems with prescribed Dirichlet boundary conditions (structure-Dirichlet and fluid-Dirichlet) on the interface, respectively. For the inner preconditioned GMRES solver, we set a relative error reduction 10^{-4} for the residual of the Jacobian problem. Each inner preconditioned GMRES iteration needs a AMG-PCG solver for the structure sub-problem and a AMG solver for the fluid sub-problem, with corresponding Dirichlet boundary conditions (structure-Dirichlet and fluid-Dirichlet) on the interface. In addition, for each inner GMRES iteration, a AMG-PCG solver for the structure sub-problem with a Neumann boundary condition (structure-Neumann) on the interface is used for preconditioning the Jacobian problem.

In the Newton based FSI solver, the stopping criteria for the AMG-PCG and AMG solvers are set by a relative residual error reduction 10^{-8} .

For a comparison, we perform the Newton and the RN preconditioned GMRES solvers with four time step sizes $\Delta t = 0.5, 0.25, 0.125, 0.0625$ ms, on the coarse and fine hybrid meshes. We set the parameter $\alpha_f = 1580$ in

Algorithm 2 Newton's method for the nonlinear interface equation

$$S_s(\lambda^k) + S_f(\lambda^k) = 0$$

1: **for** each time step $n = 1, ..., N$ **do**
2: **for** each Newton iteration $k \geq 0$ **do**
3: compute the residual

$$-(S_s(\lambda^k) + S_f(\lambda^k))$$

by solving the structure and fluid sub-problems,
4: solve the Jacobian problem

$$\left(S_s'(\lambda^k) + S_f'(\lambda^k)\right)\delta\lambda^k = -\left(S_s(\lambda^k) + S_f(\lambda^k)\right)$$

via a preconditioned GMRES solver,
5: update the displacement

$$\lambda^{k+1} = \lambda^k + \delta\lambda^k,$$

if not accurate enough, go to step 1.
6: **end for**
7: **end for**

the RN preconditioned GMRES solver. The iteration numbers of one time step for the RN preconditioned GMRES and the Newton based solvers are listed in Table 1 and Table 2, respectively, where the iteration numbers on the fine mesh are put below the numbers on the coarse mesh. These iteration numbers are needed for the corresponding relative error reductions described above.

In Fig. 5, the convergence histories for one time step using the DN, RN, RN preconditioned GMRES (RN GMRES) and Newton solvers are plotted, where we set $\Delta t = 0.25$ ms.

It is obvious to see that, in terms of iteration numbers, the Newton based FSI solver needs the fewest iterations. Compared to the standard DN solver, the iteration number of the RN solver already decreases about 90%. With the GMRES acceleration, the RN preconditioned GMRES solver needs about half of iterations from the RN solver. Since the DN and RN solvers are less

Δt	0.0625 ms	0.125 ms	0.25 ms	0.5 ms
AMG-PCG (structure-Dirichlet)	2	$2 \sim 3$	$2 \sim 3$	3
	2	2	2	2
AMG (fluid-Robin)	2	2	2	2
	1	1	1	1
AMG-PCG (structure-Neumann)	3	$4 \sim 6$	$7 \sim 9$	$9 \sim 12$
	$2 \sim 3$	$4 \sim 5$	$5 \sim 6$	$6 \sim 7$
GMRES iterations	5	3	5	5
	6	4	6	6

Table 1: Iteration numbers in the RN preconditioned GMRES solver for one time step.

Δt	0.0625 ms	0.125 ms	0.25 ms	0.5 ms
AMG-PCG (structure-Dirichlet)	12	13	$13 \sim 14$	$13 \sim 14$
	10	$10 \sim 11$	11	11
AMG (fluid-Dirichlet)	$3 \sim 4$	$3 \sim 4$	$3 \sim 4$	$3 \sim 4$
	$2 \sim 4$	$2 \sim 4$	$2 - 4$	$2 - 3$
AMG-PCG (structure-Neumann)	$18 \sim 19$	$28 \sim 30$	$42 \sim 46$	$55 \sim 59$
	13	$20 \sim 22$	$24 \sim 27$	$31 \sim 33$
Inner GMRES iterations	$10 \sim 11$	10	9	8
	11	10	$9 \sim 10$	$8 \sim 9$
Newton iterations	2	2	2	2
	2	2	2	3

Table 2: Iteration numbers in the Newton based FSI solver for one time step.

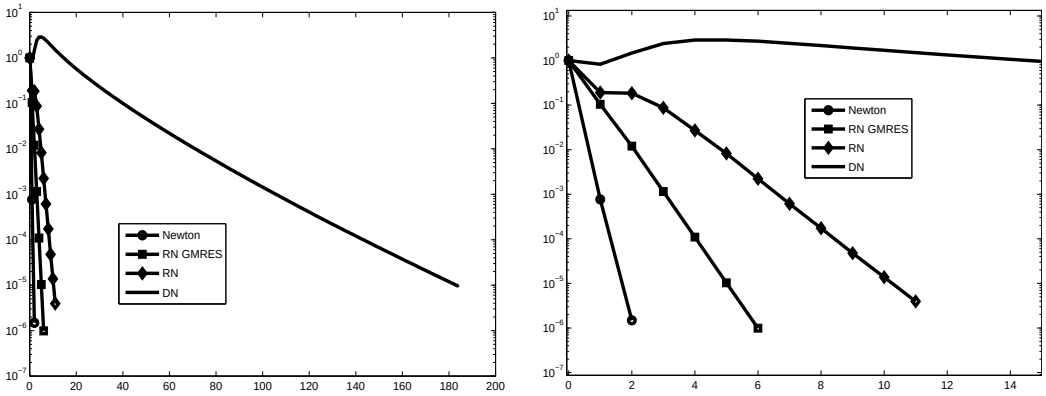

(a) Convergence histories using different solvers

(b) Convergence histories in 15 iterations using different solvers

Figure 5: Convergence histories using the DN, RN, RN GMRES and Newton solvers. The horizontal axis represents the iteration numbers, the relative residual errors are plotted in the vertical direction.

efficient compared to the other two, they will not be discussed furthermore in the following.

It is observed that for each time step, about 5 RN preconditioned GMRES iterations are needed. For each of them, 2 structure sub-problems (1 structure-Dirichlet and 1 structure-Neumann) are solved by the AMG-PCG solver, and 1 fluid sub-problem (fluid-Robin) is solved by the AMG solver, up to a relative residual error 10^{-2}. So for each time step, in total 10 structure and 5 fluid sub-problems need to be solved approximately. For the Newton based FSI solver, about 40 structure (20 structure-Dirichlet and 20 structure-Neumann) and 20 fluid (fluid-Dirichlet) sub-problems for each time step have to be solved, up to a relative residual error 10^{-8}. In sum we need to solve about 4 times as many structure and fluid sub-problems for the Newton FSI solver as structure and fluid sub-problems we need for the RN preconditioned solver. See Table 3, where the numbers of sub-problems on the fine mesh are put below the numbers on the coarse mesh.

Note that in the Newton based FSI solver, for each time step we need to assemble the finite element matrices and vectors about $2 \sim 3$ times. Rather, in the RN preconditioned GMRES solver, for each time step, only one assembly is needed. According to our numerical experiences, the assembly on hybrid meshes is quite costly.

Therefore in terms of CPU time, the RN preconditioned GMRES solver

	structure	fluid
RN GMRES	10 (5/5 structure-Dirichlet/Neumann)	5 (fluid-Robin)
	12 (6/6 structure-Dirichlet/Neumann)	6 (fluid-Robin)
Newton	40 (20/20 structure-Dirichlet/Neumann)	20 (fluid-Dirichlet)
	40 (20/20 structure-Dirichlet/Neumann)	20 (fluid-Dirichlet)

Table 3: Numbers of structure and fluid sub-problems for the RN preconditioned GMRES and the Newton based solvers on each time step.

shows its superiority to the Newton based solver. See in Table 4 the CPU time in seconds for the cost of one time step using two solvers, where the CPU time on the fine mesh is put below the time on the coarse mesh. The code is tested on a laptop with an Intel Core of 2.67 GHz and 4 GB memory.

Δt	0.0625 ms	0.125 ms	0.25 ms	0.5 ms
RN GMRES	248.57 s	242.1 s	249.28 s	250.29 s
	4751.43 s	4719.04 s	4752.87 s	4752.46 s
Newton	811.39 s	815.19 s	816.74 s	810.87 s
	14706.6 s	14645.2 s	14552.6 s	19467.7 s

Table 4: Cost of one time step using the RN preconditioned GMRES and the Newton based solvers.

It is observed that the cost of one time step is independent of the time step size for both solvers. The RN preconditioned GMRES solver is about two times more efficient than the Newton based solver.

For comparing the numerical solutions from both solvers, we use four different time step sizes $\Delta t = 0.5, 0.25, 0.125, 0.0625$ ms and run the simulation until the ending time $t = 10$ ms on the coarse mesh. The resulting pressure waves along the center line from the RN preconditioned GMRES and the Newton based solvers are compared with each other for these four time step sizes in Figure 6.

We observe that the numerical solutions from both solvers are conforming well to each other. A further refinement leads to a time step size $\Delta t = 0.03125$ ms. The corresponding pressure waves are almost identical to the

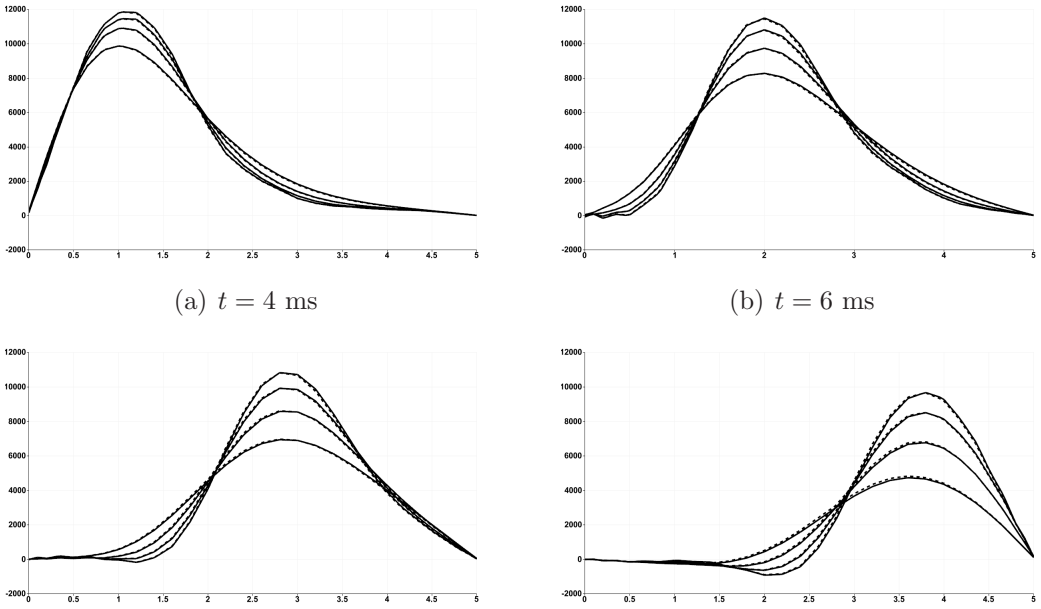

(a) $t = 4$ ms (b) $t = 6$ ms

(c) $t = 8$ ms (d) $t = 10$ ms

Figure 6: Pressure waves at different time levels with four time step sizes: $\Delta t = 0.5, 0.25, 0.125, 0.0625$ ms. The horizontal axis represents the centerline of the cylinder; the pressure is plotted in the vertical direction. The solid lines represent the RN preconditioned GMRES solutions; the dashed lines represent the Newton solutions.

results with a time step size $\Delta t = 0.0625$ ms. So, obviously, convergence with respect to the temporal discretization has been observed.

In Figure 7, we compare the pressure wave along the center line of the cylinder on the coarse mesh with that on the fine mesh, using the RN preconditioned GMRES and the Newton based solvers.

The results for both meshes are almost identical, except that the speed of the wave propagation on the fine mesh is a little bit faster than that on the coarse one. So, to some extent, also convergence with respect to the spatial discretization has been observed. It is also observed that the numerical solutions from both solvers conform well on the coarse mesh (solid/dashed lines with circles) as well as on the fine mesh (solid/dashed lines without circles).

Fig. 8 shows the deformation of the computational structure domain and the fluid velocity field on the coarse mesh at four time levels: $t = 4,\ 6,\ 8,\ 10$ ms, with the time step size $\Delta t = 0.125$ ms. For visualization purposes the deformation is amplified by a factor of 12. The results are comparable to

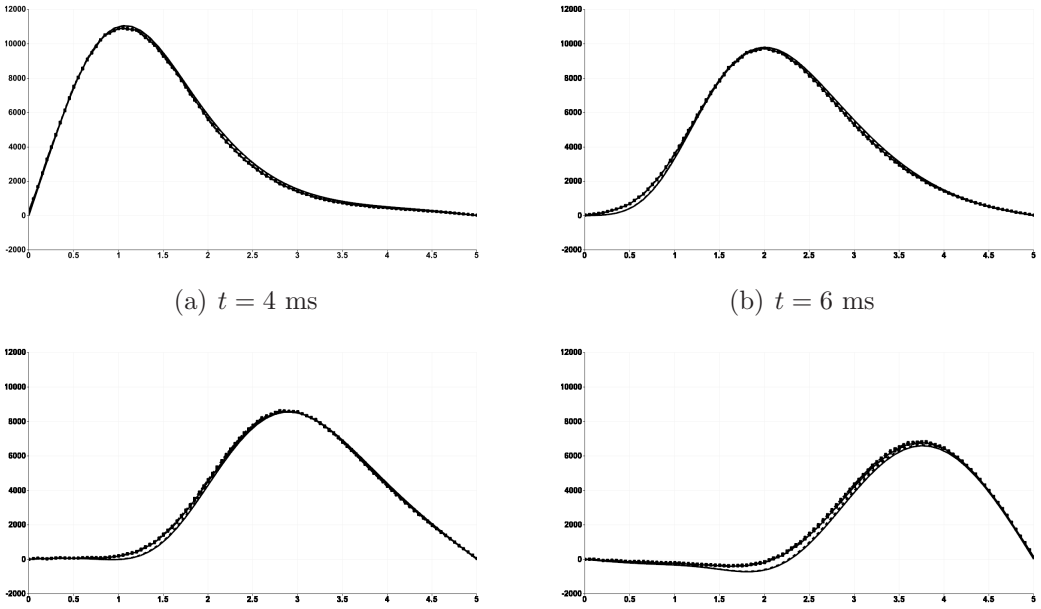

(a) $t = 4$ ms (b) $t = 6$ ms

(c) $t = 8$ ms (d) $t = 10$ ms

Figure 7: Pressure waves at different time levels with a time step size $\Delta t = 0.25$ ms, on two meshes: fine mesh (solid/dashed lines without circles) and coarse mesh (solid/dashed lines with circles). The horizontal axis represents the centerline of the cylinder; the pressure is plotted in the vertical direction. The solid lines (with and without circles) represent the RN preconditioned GMRES solutions; the dashed lines (with and without circles) represent the Newton solutions.

those given in [9, 28].

6.4. Numerical studies on the convergence dependence

Compared with the Newton based FSI solver, the RN preconditioned GMRES solver involves a Robin weighting parameter α_f that has to be chosen. In the work of [3], Santiago Badia etc. have investigated on how to choose the optimal α_f based on a simplified FSI problem. However, in general it is difficult to analyze this for the FSI problem on a complicated computational domain. Rather, in this work, the feasibility of the RN preconditioned GMRES solver is verified by numerical studies.

For this, some numerical experiments are performed for studying the convergence dependence on different parameters: the Robin weighting parameter α_f, the time step size Δt, the thickness h_s of the structure wall, the ratio

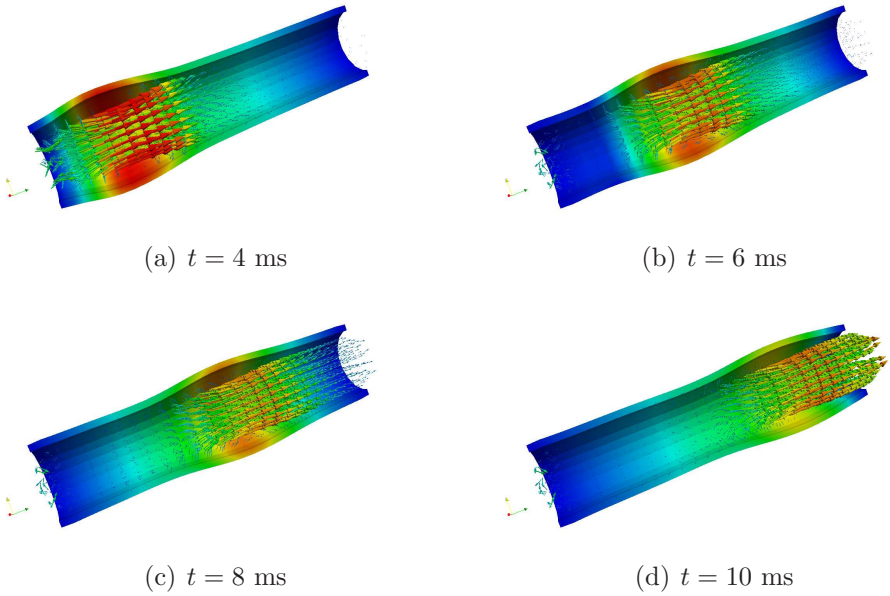

(a) $t = 4$ ms (b) $t = 6$ ms

(c) $t = 8$ ms (d) $t = 10$ ms

Figure 8: The visualization of the deformation of the structure domain and the fluid velocity fields on the coarse mesh at four time levels $t = 4, 6, 8, 10$ ms.

ρ_s/ρ_f of the structure density over the fluid density, and the slenderness $sl = \frac{L}{D}$ of the computational FSI domain, where L and D are the length and the diameter of the computational domain.

Note that in the following plots of convergence histories with different choices of parameters, the horizontal axis represents the iteration numbers of the RN preconditioned GMRES solver, and the relative residual errors are plotted in the vertical direction. The convergence histories for different choices of each parameter are indicated with corresponding line styles.

In the following, we only show the results of the simulations running on the coarse hybrid mesh. We observe similar results on the fine hybrid mesh. Since convergence histories behave in the same way for all time steps, we only plot the convergence histories for one time step.

6.4.1. Dependence on α_f

To see the convergence dependence on the Robin weighting parameter α_f, we fix the time step size $\Delta t = 0.25$ ms and all the other parameters, but change α_f by factors of 0.1 and 10. The convergence histories for one time step are plotted in Fig. 9(a) for three choices of $\alpha_f = 1580,\ 158,\ 15800$.

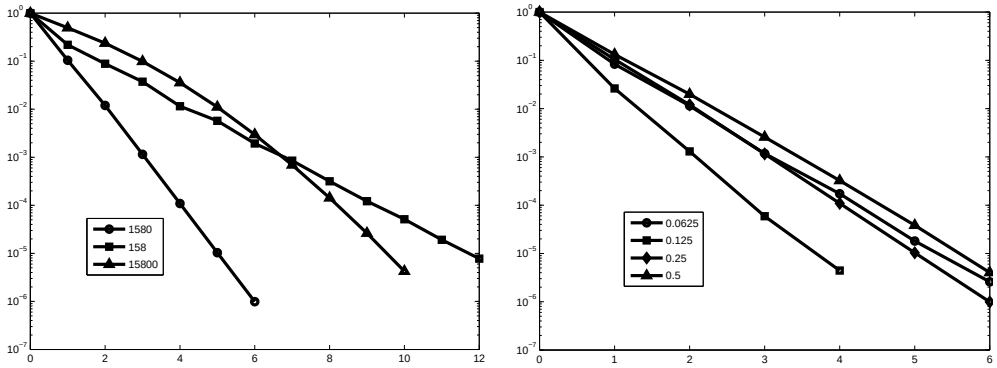

(a) Convergence history with varying α_f. (b) Convergence history with varying Δt.

Figure 9: Convergence dependence on α_f and Δt

We observe that the choice $\alpha_f = 1580$ corresponds to an optimal one for our specified FSI problem. The iteration numbers are increasing but still acceptable with choices of $\alpha_f = 158,\ 15800$, which are comparable to the results from [3]. If we decrease or increase α_f further, more iteration numbers are needed. In the limit case $\alpha_f = 0$ and $\alpha_f = +\infty$, we have the NN preconditioned and DN preconditioned GMRES solvers, respectively. Both suffer from the added-mass effect.

6.4.2. Dependence on Δt

The dependence on Δt has been reflected in Table 1. We fix the Robin weighting parameter $\alpha_f = 1580$. The convergence histories for one time step with different time step sizes $\Delta t = 0.5,\ 0.25,\ 0.125,\ 0.0625$ ms are plotted in Fig. 9(b).

One easily sees that for this particular choice of α_f, the RN preconditioned GMRES solver convergences a little bit faster using smaller time step sizes. It is notable that for the inner GMRES solver in each Newton iteration, the number of iterations increases with decreasing time step sizes (see the iteration numbers of the inner GMRES solver in Table 2), which is also observed in [9].

6.4.3. Dependence on h_s

We fix $\alpha_f = 1580$ and $\Delta t = 0.25$ ms, but vary the thickness of the wall $h_s = 1,\ 0.5,\ 0.25$ mm, see Fig. 10 for the cross sections of the computational domains. The iteration numbers for each choice of h_s are plotted in Fig.

11(a).

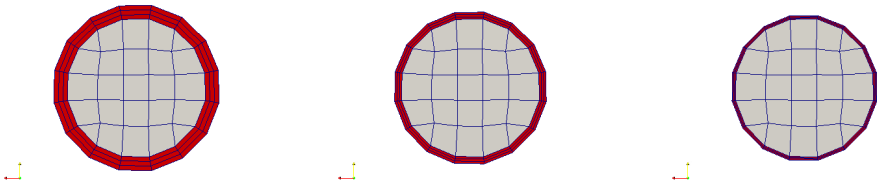

(a) $h_s = 1$ mm (b) $h_s = 0.5$ mm (c) $h_s = 0.25$ mm

Figure 10: Three choices of the thickness of the surrounding structure.

It is observed that for the thinner structure walls, more RN preconditioned GMRES iterations are needed. For a further thinner wall, we are running into a stability problem from the structure discretization, which is considered as a future work. So far, we have not faced so thin structures from practical applications.

6.4.4. Dependence on sl

We fix $\alpha_f = 1580$ and $\Delta t = 0.25$ ms, but vary the slenderness $sl \approx 5.0$, 10.0, 20.0 of the computational domain, see Fig. 12. The convergence history for each choice is plotted in Fig. 11(b).

One easily sees that the iteration numbers of the RN preconditioned GMRES solver stay in a similar range for different choices of sl.

6.4.5. Dependence on ρ_s/ρ_f

We fix $\Delta t = 0.25$ ms, but vary the ratio $\rho_s/\rho_f = 1.2$, 12, 120, 1200 of the structure density over the fluid density. The convergence histories are plotted in Fig. 13(a) and Fig. 13(b) for $\alpha_f = 1580$ and $\alpha_f = 15800$, respectively.

It is observed that for the RN preconditioned GMRES solver with the choice $\alpha_f = 1580$, more iterations of the GMRES solver are needed for larger ratios ρ_s/ρ_f, see Fig. 13(a). However, for the choice $\alpha_f = 15800$, the convergence for larger ratios ρ_s/ρ_f improves, see Fig. 13(b). For the latter choice, it is closer to the DN preconditioned GMRES solver. As is well known the DN solver works well for large ratios ρ_s/ρ_f, but not for the ratio $\rho_s/\rho_f \approx 1$ due to the added-mass effect.

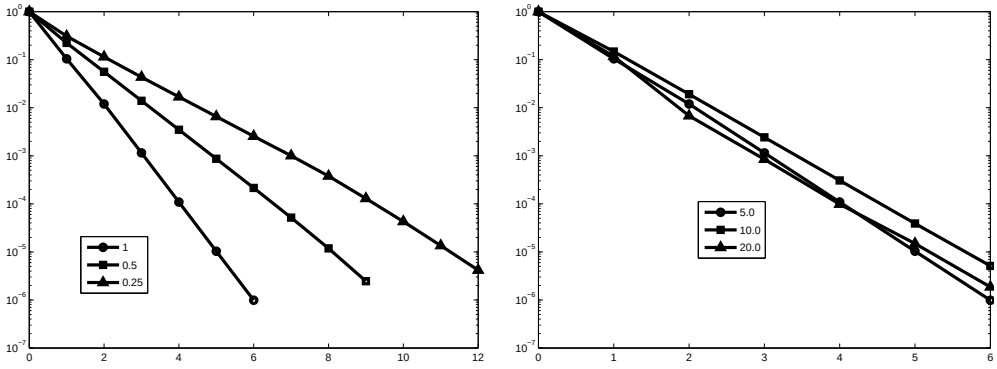

(a) Convergence history with varying h_s. (b) Convergence history with varying sl.

Figure 11: Convergence dependence on h_s and sl

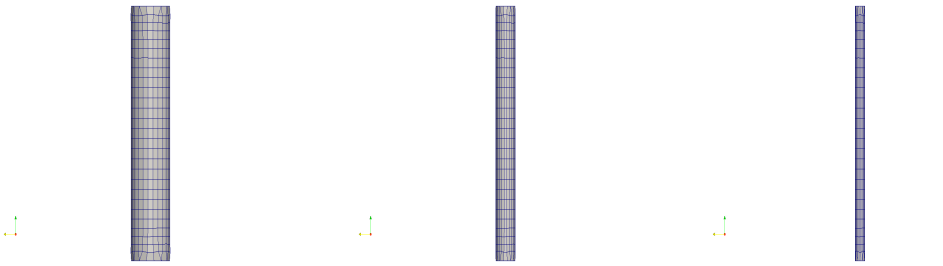

(a) $sl \approx 5.0$ (b) $sl \approx 10.0$ (c) $sl \approx 20.0$

Figure 12: Computational domains with different slenderness sl.

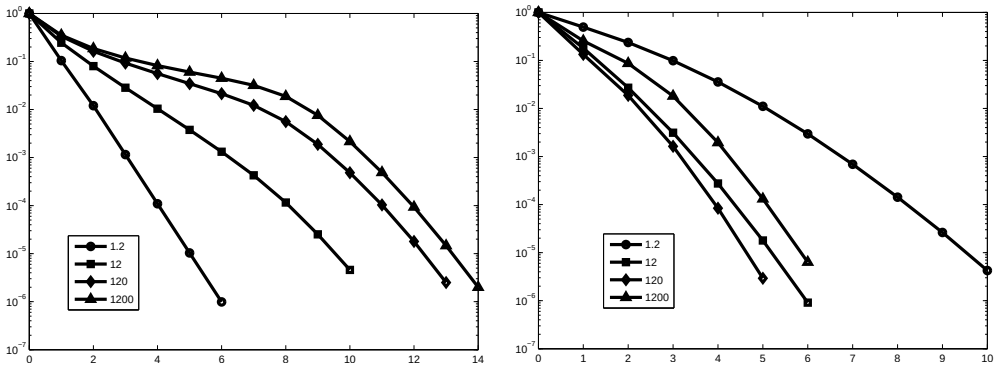

(a) Convergence history with varying ρ_s/ρ_f. (b) Convergence history with varying ρ_s/ρ_f.

Figure 13: Convergence dependence on ρ_s/ρ_f: $\alpha_f = 1580$ (left) and $\alpha_f = 15800$ (right).

6.5. A comparison of numerical solutions on a hybrid mesh to those on a tetrahedral mesh

We compare the numerical solutions on a tetrahedral mesh containing $3,942$ vertices and $19,512$ tetrahedral elements ($13,144$ structure elements and $6,368$ fluid elements, see Fig. 14), with the solutions on the previously used coarse hybrid mesh containing $4,176$ vertices and $3,965$ hybrid elements ($1,944$ structure elements and $2,021$ fluid elements).

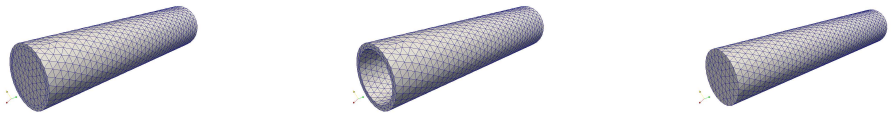

(a) tetrahedral mesh (b) $13,144$ elements (c) $6,368$ elements

Figure 14: The pure tetrahedral mesh for the FSI computational domain.

One easily sees that both meshes have similar numbers of degrees of freedom (vertices), but the number of hybrid elements is about 20% of the number of tetrahedral elements.

The pressure wave propagations along the center line on the tetrahedral and hybrid meshes are plotted in Fig. 15.

Up to the spatial discretization errors, the pressure waves on both meshes conform well to each other. The pressure wave propagates a little bit faster on the hybrid mesh than that on the tetrahedral mesh.

7. Conclusions and future works

This paper has presented a RN preconditioned GMRES solver for the Schur complement equation (formulated in terms of the structure displacement on the interface) of the coupled FSI system, for which special AMG solvers are used to solve the structure and fluid sub-problems discretized on hybrid meshes. It is compared with our previously developed Newton based FSI solver and shows some advantages concerning the CPU time. The convergence dependence on different parameters is tested by performing selected numerical examples, which demonstrate the feasibility of this solver. The rigorous convergence analysis for a general FSI model is an ongoing work.

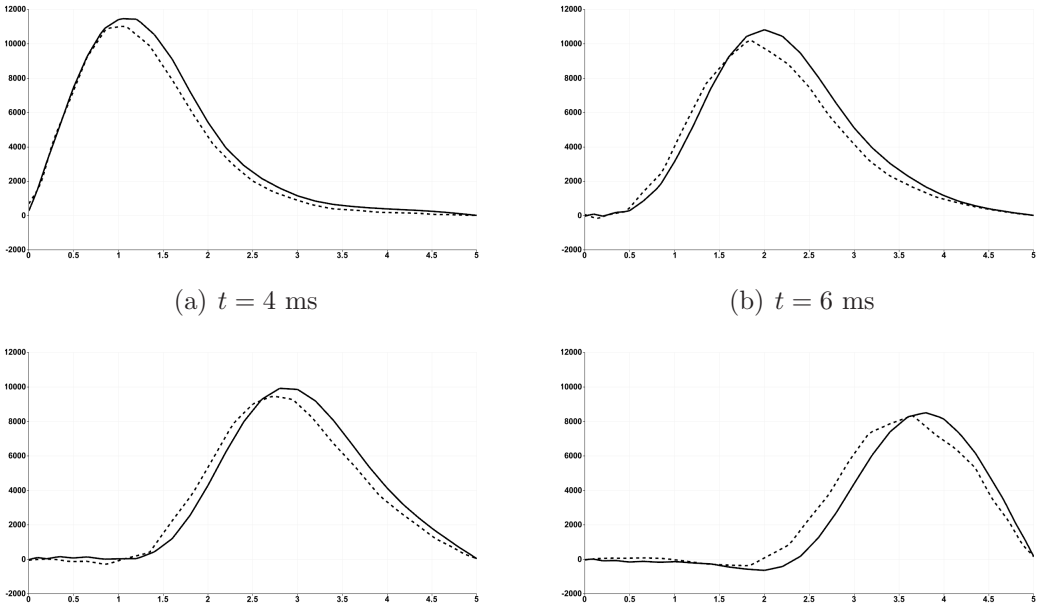

(a) $t = 4$ ms (b) $t = 6$ ms

(c) $t = 8$ ms (d) $t = 10$ ms

Figure 15: A comparison of pressure waves on the hybrid mesh to that on the tetrahedral mesh at different time levels with the time step size: $\Delta t = 0.125$ ms. The horizontal axis represents the centerline of the cylinder; the pressure is plotted in the vertical direction. The solid lines represent the solutions on the hybrid mesh; the dashed lines represent the solutions on the tetrahedral mesh.

References

[1] R. A. Adams and J. J. F. Fournier. *Sobolev Spaces*, volume 140 of *Pure and Applied Mathematics*. Academic Press, Amsterdam, Boston, second edition, 2003.

[2] S. Badia, F. Nobile, and C. Vergara. Fluid-structure partitioned procedures based on Robin transmission conditions. *Journal of Computational Physics*, 227:7027–7051, 2008.

[3] S. Badia, F. Nobile, and C. Vergara. Robin-Robin preconditioned Krylov methods for fluid-structure interaction problems. *Comput. Methods Appl. Mech. Engrg.*, 198:1768–2784, 2009.

[4] A. Barker and X.-C. Cai. Scalable parallel methods for monolithic cou-

pling in fluid-structure interaction with application to blood flow modeling. *J. Comput. Phys.*, (229):642–659, 2010.

[5] D. Braess and R. Sarazin. An efficient smoother for the Stokes problem. *Appl. Numer. Math.*, 23:3–19, 1997.

[6] F. Brezzi and M. Fortin. *Mixed and Hybrid Finite Element Methods*. Springer series in computational mathematics. Springer, New York, 1991.

[7] A. N. Brooks and T. J. R. Hughes. Streamline upwind/Petrov-Galerkin formulation for convection dominated flows with particular emphasis on the incompressible Navier-Stokes equations. *Comput. Methods Appl. Mech. Engrg.*, 32:199–259, 1982.

[8] P. Causin, J. F. Gerbeau, and F. Nobile. Added-mass effect in the design of partitioned algorithm for fluid-structure problems. *Comp. Meth. Appl. Mech. Eng.*, 194:4506–4527, 2005.

[9] S. Deparis, M. Discacciati, G. Fourestey, and A. Quarteroni. Fluid-structure algorithms based on Steklov-Poincaré operators. *Comput. Methods Appl. Mech. Engrg.*, 195:5797–5812, 2006.

[10] M. A. Fernández and M.Moubachir. A Newton method using exact Jacobians for solving fluid-structure coupling. *Comput. & Struct.*, 83(2-3):127–142, 2005.

[11] L. Formaggia and F. Nobile. A stability analysis for the arbitrary Lagrangian Eulerian formulation with finite elements. *East-West Journal of Numerical Mathematics*, 7:105–132, 1999.

[12] C. Förster. *Robust methods for fluid-structure interaction with stabilised finite elements*. PhD thesis, University Stuttgart, 2007.

[13] L.P. Franca and T.J.R. Hughes. Two classes of mixed finite element methods. *Computer Methods in Applied Mechanics and Engineering*, 69:89–129, 1998.

[14] V. Girault and P.A. Raviart. *Finite Element Methods for Navier-Stokes Equations: Theory and Algorithms*. Springer, New York, 1985.

[15] M. Griebel, D. Oeltz, and M. A. Schweitzer. An algebraic multigrid method for linear elasticity. *SIAM. J. Sci. Comput.*, 25:385–407, 2003.

[16] F. Kickinger. Algebraic multigrid for discrete elliptic second-order problems. In *Multigrid Methods V. Proceedings of the 5th European Multigrid conference (ed. by W. Hackbush), Lecture Notes in Computational Sciences and Engineering, vol. 3*, pages 157–172. Springer, 1998.

[17] U. Küttler and Wolfgang A. Wall. Fixed-point fluid-structure interaction solvers with dynamic relaxation. *Comput Mech*, 43:61–72, 2008.

[18] U. Langer, H. Yang, and W. Zulehner. Numerical simulation of fluid-structure interaction problems on the grid environment. In J. Volkert, T. Fahringer, D. Kranzlmüller, R. Kobler, and W. Schreiner, editors, *Proceedings of 3rd Austria Grid Symposium*, pages 13–27. OCG publisher, Vienna, 2010.

[19] T. J. R.Hughes, L. P. Franca, and M. A. Balestra. A new finite element formulation for computational fluid dynamics: V. Circumventing the BabuškaBrezzi condition: A stable PetrovGalerkin formulation of the Stokes problem accommodating equal order interpolations. *Comput. Method Appl. Mech. Engrg.*, 59:85–99, 1986.

[20] J. W. Ruge and K. Stüben. Algebraische mehrgittermethodenalgebraic multigrid (AMG). In *Multigrid Methods*, volume 3 of *Frontiers in Applied Mathematics*, pages 73–130. SIAM, Philadelphia, 1987.

[21] Y. Saad and M. H. Schultz. Gmres : A generalized minimal residual algorithm for solving nonsymmetric linear system. *SIAM J. Sci. Stat. Comput.*, 7:856–869, 1986.

[22] M. Wabro. *Algebraic Multigrid Methods for the Numerical Solution of the Incompressible Navier-Stokes Equations*. PhD thesis, Johannes Kepler University Linz, 2003.

[23] M. Wabro. Coupled algebraic multigrid methods for the oseen problem. *Comput. Vis. Sci.*, 7:141–151, 2004.

[24] M. Wabro. AMGe—coarsening strategies and application to the Oseen equations. *SIAM J. Sci. Comput.*, 27:2077–2097, 2006.

[25] H. Yang. *Numerical Simulation of Fluid-Structure Interaction Problems on Hybrid Meshes with Algebraic Multigrid Methods*. PhD thesis, Johannes Kepler University Linz, 2010.

[26] H. Yang and W. Zulehner. Numerical simulations of fluid-structure interaction problems on hybrid meshes with algebraic multigrid methods. In I. Lirkov, S. Margenov, and J. Wasniewski, editors, *Large-Scale Scientific Computing*, pages 116–123, Berlin, Heidelberg, 2010. Springer.

[27] H. Yang and W. Zulehner. A Newton based fluid-structure interaction solver with algebraic multigrid methods on hybrid meshes. In Y. Huang, R. Kornhuber, O. Widlund, and J. Xu, editors, *Domain Decomposition Methods in Science and Engineering*, pages 285–292. Springer, 2011.

[28] H. Yang and W. Zulehner. Numerical simulation of fluid-structure interaction problems on hybrid meshes with algebraic multigrid methods. *Journal of Computational and Applied Mathematics*, 2011. doi:10.1016/j.cam.2011.05.046.

[29] W. Zulehner. A class of smoothers for saddle point problems. *Computing*, 65:227–246, 2000.